

# Diamond Devices for High Acuity Prosthetic Vision

Arman Ahnood, Hamish Meffin, David J. Garrett,\* Kate Fox, Kumaravelu Ganesan, Alastair Stacey, Nicholas V. Apollo, Yan T. Wong, Samantha G. Lichter, William Kentler, Omid Kavehei, Ursula Greferath, Kirstan A. Vessey, Michael R. Ibbotson, Erica L. Fletcher, Anthony N. Burkitt, and Steven Prawer

Retinal implants restore a sense of vision, for a growing number of users worldwide. Nevertheless, visual acuities provided by the current generation of devices are low. The quantity of information transferable to the retina using existing implant technologies is limited, far below receptor cells' capabilities. Many agree that increasing the information density deliverable by a retinal prosthesis requires devices with stimulation electrodes that are both dense and numerous. This work describes a new generation of retinal prostheses capable of upscaling the information density conveyable to the retina. Centered on engineered diamond materials, the implant is very well tolerated and long-term stable in the eye's unique physiological environment and capable of delivering highly versatile stimulation waveforms – both key attributes in providing useful vision. Delivery of high-density information, close to the retina with the flexibility to alter stimulation parameters in situ provides the best chance for success in providing high acuity prosthetic vision.

## 1. Introduction

In the last decade, retinal prostheses have moved out of the realm of science fiction, and into the hands of surgeons and the eyes of patients. Two organizations have had led the charge, namely Second Sight, whose Argus II device is approved for use in North America and Europe and Retina Implant AG's Alpha IMS system, which has obtained approval in Europe. The enormous complexity of the human visual system, with 130 million photoreceptor cells, 1.2 million retinal ganglion cells, and layers of information processing involves in making sense of what we see. In parallel, the importance of the materials used to manufacture effective, safe, long-lasting implants and projected on the role of emerging technologies to increase

the visual acuity provided by retinal implants has been long sought after.<sup>[1]</sup> In recent years, several groups including Second Sight with the Argus II,<sup>[2]</sup> Retina Implant AG's Alpha IMS,<sup>[3]</sup> and Bionic Vision Australia (BVA) with their suprachoroidal device<sup>[4]</sup> have demonstrated that retinal implants can restore a sense of vision in some patients, but that the visual acuity is below the requirement threshold for functional vision.<sup>[5]</sup> What visual acuity and function could retinal prostheses provide to patients and what do we need to build to achieve the best possible functional acuity?

Retinal stimulation devices are of potential benefit to people with retinal diseases such as retinitis pigmentosa (RP), which results in a loss of photoreceptors within the retina (the rods and cones), while a significant proportion of the ganglion cells, bipolar cells, and other neuronal elements remain viable and responsive to electrical stimulation. Electrical stimulation of surviving retinal neurons results in neuron activation and signal translation through the optic nerve to the visual cortex.<sup>[6]</sup> Participants report that the stimulated location on the retina is perceived as a shape in the visual field, commonly called a phosphene.<sup>[6]</sup> The shapes can be single spots but their morphology is often more complex. Retinal prostheses are typically positioned either under the retina (subretinal), on top of the retina (epiretinal), or as reported recently, between the choroid and the sclera (suprachoroidal).<sup>[7–9]</sup> We show the general anatomy of the retina (**Figure 1**) and an enlarged drawing of the outer layers of the eye that support and protect the retina (**Figure 1a**),

Dr. A. Ahnood, Dr. D. J. Garrett, Dr. K. Fox,  
Dr. K. Ganesan, Dr. A. Stacey, N. V. Apollo,  
Dr. S. G. Lichter, Prof. S. Prawer  
School of Physics  
University of Melbourne  
Victoria 3010, Australia  
E-mail: dgarrett@unimelb.edu.au



Dr. H. Meffin, Dr. Y. T. Wong, Prof. M. R. Ibbotson  
National Vision Research Institute  
Australian College of Optometry  
Victoria 3053, Australia

Dr. H. Meffin, Prof. M. R. Ibbotson  
ARC Centre of Excellence for Integrative Brain Function  
Department of Optometry and Vision Science  
University of Melbourne  
Victoria 3010, Australia

Dr. K. Fox, Dr. O. Kavehei  
School of Engineering  
RMIT University  
Melbourne 3000, Australia

Dr. Y. T. Wong, W. Kentler, Prof. A. N. Burkitt  
Department of Electrical & Electronic Engineering  
The University of Melbourne  
Victoria 3010, Australia

Dr. U. Greferath, Dr. K. A. Vessey, Prof. E. L. Fletcher  
Department of Anatomy and Neuroscience  
University of Melbourne  
Victoria 3010, Australia

DOI: 10.1002/adbi.201600003

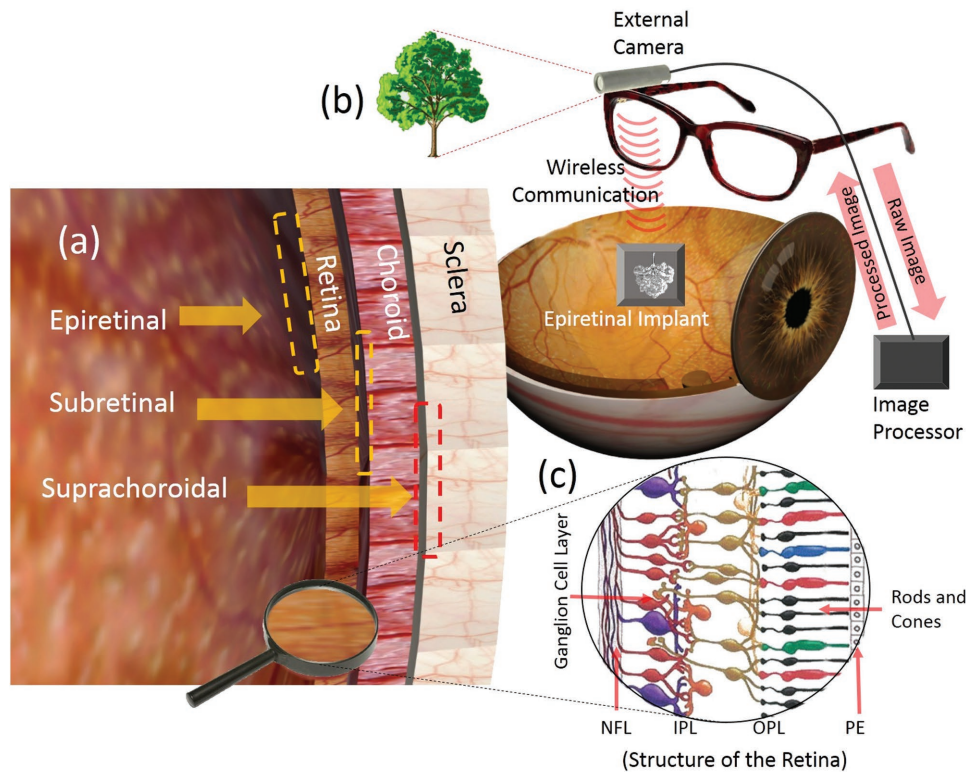


**Figure 1.** Overview of the epiretinal device placement strategy adopted for the diamond based retinal stimulator presented in this work (diagram is not to scale). a) Gross structure of the wall of the eye showing the three most common implant positions, i.e., epiretinal, subretinal, and suprachoroidal. b) Schematic diagram of an epiretinal implant showing external components and c) the structure of the retina indicating the ganglion cell layer, the nerve fiber layer (NFL), the inner plexiform layer (IPL), the outer plexiform layer (OPL), the rods and cones, and the pigment epithelium (PE).

highlighting the location of the various device placements. Image information is often captured by an external device, usually a camera (e.g., Argus II and BVA), and transferred to a processing unit. The raw image is processed and sent to the implant as a series of electrical stimulus parameters for each of the electrodes on the array. Alternatively, image data can be captured inside the eye by means of a photodiode array on the retinal prosthesis (e.g., Alpha IMS<sup>[10]</sup>). Provided that the person using the device has a working retinal ganglion cell network and a developed visual pathway, patterns of stimulation on the retina are mapped spatiotopically to the visual cortex. The quality of the image perceived by the patient is a function of the number, size, and shape of the elicited phosphenes and how clearly and distinctly those phosphenes are perceived.

Currently, all the leading retinal prostheses operate via direct electrical stimulation of the retina using an array of electrodes, with the electrodes themselves driven electrically or optically. Beyond electrical stimulation, retinal stimulation has been demonstrated using methods based on optogenetics<sup>[11,12]</sup> and photochemical switching.<sup>[13,14]</sup> Common hallmarks of these approaches are their potential to restore high acuity vision as specific neuron types can be selectively targeted with millisecond accuracy without fading of responses over long-time frames. Current technologies also allow for finer control over the size of light used for stimulation in optogenetics as opposed to the size of the spread of current in electrical stimulation.<sup>[15]</sup> However, neurotoxicity, immunogenicity, and long-term

stability in the retina<sup>[16]</sup> of these approaches are currently under active investigation. Therefore, lower risks associated with electrical stimulation of retina using retinal prostheses have accelerated their adoption as a therapeutic method.

In striving for higher acuity prosthetic vision, the most logical direction, and the one that the majority of retinal prosthesis developers have taken, is toward devices with arrays of electrodes that are more numerous, smaller, and denser, thus increasing the spatial information delivered to the retina.<sup>[17]</sup> As implants' electrode density and count progressively scales toward that of receptor cells, it becomes increasingly difficult to fabricate devices using traditional methods and alternative strategies are required.

Using nanostructured diamond electrodes, monolithically integrated with polycrystalline diamond housing, an implant with a high electrode density and count is reported in this work, which simultaneously satisfies biocompatibility and biostability concerns through the use of its all-diamond electrode array. A second pivotal requirement is that the electrode array and housing be suitable for the hermetic encapsulation of implanted electronic circuitries which are used to drive the individual stimulating electrodes. Owing to its high chemical<sup>[18]</sup> and biochemical stability, and excellent biocompatibility profile,<sup>[19–21]</sup> diamond has been considered as a long-lasting, bioinert encapsulation material<sup>[22,23]</sup> in medical implants.<sup>[24]</sup> Beyond these highly advantageous attributes, the atomic structure of diamond yields an outstanding nonpermeable barrier

which enables the realization of hermetic encapsulation for long-term implantable electronics. The high-density monolithic integration of conductive nitrogen doped ultrananocrystalline diamond (N-UNCD) electrode channels by directly depositing them within electrically insulating diamond substrates<sup>[25]</sup> has enabled hermetic all-diamond electrode array. Here, we describe a device with 256 diamond electrodes, each  $120 \times 120 \mu\text{m}$  in size separated by  $30 \mu\text{m}$  trenches, yielding an electrode pitch of  $150 \mu\text{m}$ . While this pitch was dictated by the design of the current generation of a highly versatile application-specific integrated circuit (ASIC) and is by no means a lower limit on the diamond electrode fabrication process. In principle, the fabrication process allows the pitch to be reduced by one order of magnitude, resulting in thousands of electrodes within a  $2.4 \times 2.4 \text{ mm}$  array.

While increasing the electrode density is a prerequisite for high acuity vision, it is not in itself sufficient. The Alpha IMS is a case in point. It has 1500 electrodes at a pitch of  $70 \mu\text{m}$ , but the Alpha IMS in clinical trials provides similar visual acuity to the Argus II system, which features just 60 electrodes separated by more than  $500 \mu\text{m}$ .<sup>[2,10]</sup> The 60 electrodes of the Argus II are individually controlled, thus providing flexibility of stimulation, whereas the Alpha IMS system electrodes are controlled by on-chip photodiodes, responding to light arriving naturally on the retina. The subretinal photodiode approach has some significant advantages. Most notably, these include the stability of the subretinal location and circumventing problems associated with the disconnect between normal eye movements and an externally captured (fixed) image. The direct control of the stimulating electrodes using photodiodes limits the versatility and adaptability of the implant in terms of stimulus parameters and the ability to employ image processing to alter the way information is presented at the retina. Although significant progress has been made to enhance capabilities of photodiode controlled electrodes, notably works led by Palanker and co-workers,<sup>[26,27]</sup> the absence of an on-board microprocessor results in some of these limitations remaining. For instance, stimulation pulses which are charge balanced (i.e., zero net-charge is injected by the electrode) are thought to be an important aptitude for effective long-term stimulation of neuronal cells.<sup>[28]</sup> While the photodiode controlled electrodes have been shown to achieve this within low voltage values,<sup>[29]</sup> the use of microprocessor controlled electrodes removes this restriction. Another example is the time delay between the positive and negative current pulses (interphase gap), where it has been shown the influence stimulation efficacy.<sup>[30]</sup> While the current generations of photodiode controlled electrodes do not currently offer this capability,<sup>[29]</sup> their microprocessor controlled counterparts do. These differences are because photodiode controlled electrodes rely on the passive capacitive charge/discharge mechanism at electrode–electrolyte interface to maintain the charge balance,<sup>[29]</sup> while the electrodes directly controlled using microprocessors actively inject positive and negative current pulses with predetermined values to maintain the charge balance and time delay.

It is possible that the visual acuity that is achievable via retinal stimulation is limited by the structure of the retina itself or by the spread of current within the retina, and increasing electrode density may provide little advantage. It is also possible

that more sophisticated stimulus patterns, the use of image processing techniques, and implementing current steering methods could result in significant improvements to visual acuity. One of the key lessons learned through the development of cochlear implants is that a wide parameter space with which to iteratively improve the stimulation strategy, combined with sophisticated speech processing, is extremely important<sup>[31]</sup> and has resulted in cochlear implant technology, far exceeding many early predictions in terms of patient outcomes.

This article demonstrates a world-first diamond encapsulated implant featuring a hermetic diamond array with 256 fully reprogrammable electrodes. The broad parameter space provided by the device in terms of stimulation flexibility makes it an ideal test substrate for evaluating the potential for generating high acuity prosthetic vision via electrical stimulation.

## 2. Overview of the Device and Surgical Approach

The diamond retinal prosthesis is illustrated pictorially in **Figure 2** in position within the eye and in an exploded view. The device consists of two components implanted during separate surgeries. The first is a suprachoroidal component containing a magnet that is implanted between the sclera and the choroid, via a scleral incision. This component is very similar in shape, size, and mechanical properties to the BVA suprachoroidal retinal prosthesis, which has been previously described<sup>[9]</sup> and has undergone successful clinical trials.<sup>[4]</sup> The second component is the diamond epiretinal prosthesis, which is implanted into the eye via a full thickness pars plana incision.<sup>[32]</sup> The epiretinal component contains the ASIC encapsulated by the hermetic diamond capsule which includes a diamond electrode array as one of its faces. Both the epiretinal and suprachoroidal components contain a parylene-coated neodymium magnet with thickness and diameter of  $3 \text{ mm}$  and  $300 \mu\text{m}$ , respectively. The suprachoroidal implant location has been shown to be highly stable in cat and human retinas.<sup>[9]</sup> Therefore, this component would always be positioned first, such that the suprachoroidal magnet lies beneath the macula, the region in human retina responsible for high-acuity vision. The encapsulated ASIC requires three wires to supply power and to transfer data to and from the chip. For the current generation of devices, these wires are routed out of the eye to an extraocular connector. Further information on the placement and system strategy adopted is presented in Section S1 in the Supporting Information.

## 3. Stimulators, Drivers, and Controller

A  $3 \times 3 \text{ mm}$  chip is fabricated in standard  $65 \text{ nm}$  complementary metal oxide semiconductor technology node with  $300 \mu\text{m}$  thickness. The ASIC device features 256 individual electrode outputs, stimulators, and their associated drivers, while facilitating highly flexible stimulation strategies through its on-board controller circuitry.<sup>[33]</sup> As well as allowing an absolute freedom in electrode selection and simultaneous stimulation with independent amplitudes at each of the 256 electrodes, the ASIC's controller supports various stimulation configurations including monopolar, bipolar, and current steering.

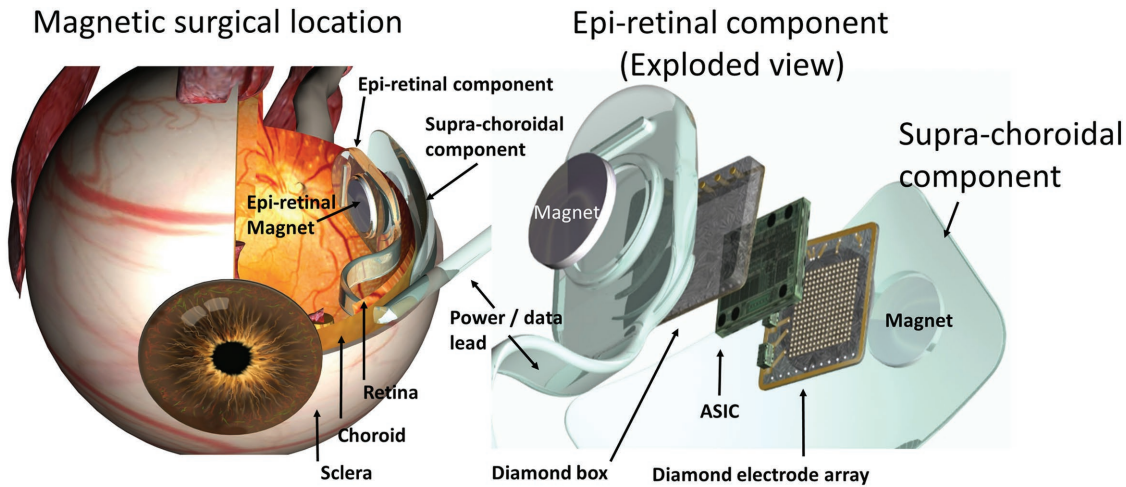


**Figure 2.** Surgical location of the suprachoroidal components (between sclera and choroid) and the epiretinal components of the retinal prosthesis. Shown adjacent is an exploded view of the epiretinal component comprising a magnet, a silicone housing, a diamond box, the stimulator ASIC, and the diamond electrode array. The suprachoroidal component and magnet are also shown.

Furthermore, variable stimulation rate and dynamic current-copying techniques are implemented to enhance the stimulation flexibility of the ASIC. The ASIC device ensures that highly precise charge delivery and charge balancing are maintained through accurate timing of current pulses and electrode shorting after each stimulation cycle. Further information on the electronic parts of the implant, including the stimulator chip and its building blocks is presented in the Supporting information.

#### 4. Device Components and Assembly

Figure 3 shows a pictorial view of the diamond capsule and microscope, and scanning electron images of the various components. The result of integrating the ASIC with the diamond electrode array is an implant which offers a flexible digital

customization and high electrode density. Flip-chip bonding the ASIC directly to the array also negates the need for a cable to connect the array to remote stimulation electronics. Fabrication and connection of a 256 wire cable, within the confines of the eye, would have presented a significant technical challenge and there is currently no clear path to scaling such a cable toward higher electrode counts, should they be desired. Flip-chip bonding is a robust, mature technology and is routinely used to address many thousands of interconnects in consumer electronic products. As the diamond electrode array is also hermetic, it can be used to encapsulate stimulating electronics. This solves the difficult problem of providing 256 high-density hermetic electrical feedthroughs to the electronics, which is critical to the long-term viability of the device inside the eye.

Scanning electron microscope (SEM) images of the  $16 \times 16$  array of diamond electrodes, higher magnification images of electrodes and a very high magnification of the nanostructured

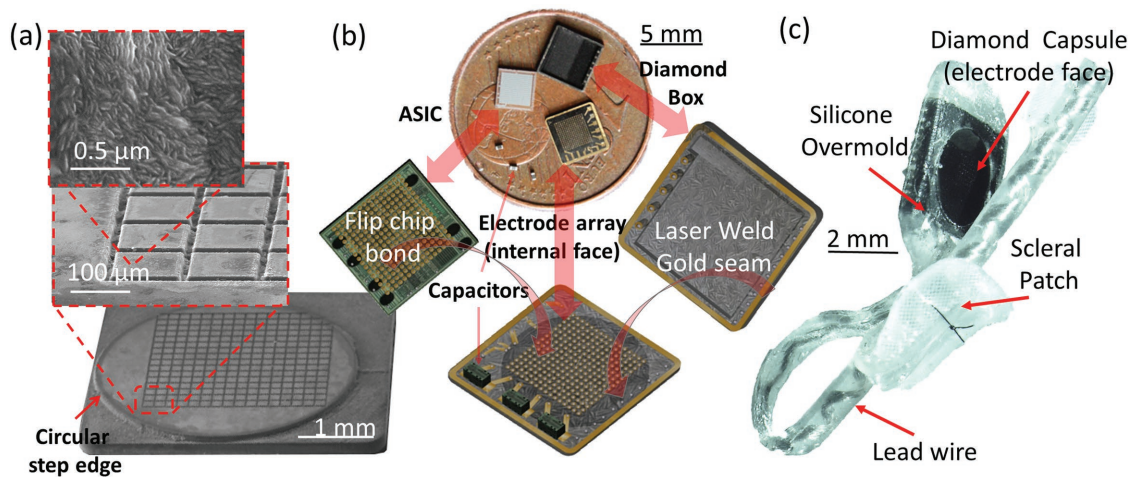


**Figure 3.** Components of the diamond based epiretinal stimulator at length scales of  $10^{-9}$ – $10^{-3}$  m. a) SEM images of the diamond electrode array at three increasing magnifications highlighting its nanostructure surface. b) Illustration and microscope images of the diamond parts, the ASIC, and capacitors of the epiretinal component. c) The complete epiretinal component indicating the silicone overmold, lead wire, and scleral patch.

diamond surface are shown in Figure 3a. Fabrication and electrochemical characterization of the diamond feedthrough and electrode array has been previously described.<sup>[25]</sup> The nanostructured surface of the diamond electrodes leads to enhanced charge injection capacity, thus allowing a low power stimulator, operating within the safe operating voltages. Figure 3b shows the internal faces of an electrode array, the diamond box, and a stimulator ASIC resting on a one Euro cent coin, with an illustration of how the components fit together. The electrodes are raised on a circular step to better fit the device to the curvature of the retina (Figure 3a). The internal faces of the diamond array and diamond box feature gold pads, internal wires, and a seam of gold around the edge for welding purposes.<sup>[34,35]</sup> Three capacitors are soldered to the array's internal face and the ASIC is connected by indium flip-chip bonding. Finally, the diamond box is fixed to the array face by laser welding together each of the Au-active braze alloy (ABA) seams on the box and the array. The feedthroughs for power and data are also formed from gold braze and penetrate through the back of the diamond box. Figure 3c shows a finished epiretinal component, complete with lead wire, silicone overmolding, and scleral patch. The biocompatible silicone overmold, which covers to edges of the implant and not the electrode face, protects the retina by preventing direct mechanical contact between the rigid diamond capsule's edges and the retinal tissue.

A partially assembled device, consisting of the 256 diamond electrode array flip-chip bonded to an ASIC ( $3 \times 3$  mm)<sup>[36]</sup> and soldered to three capacitors ( $0.3 \times 0.6$  mm), is shown in Figure 4a. The diamond encapsulation was completed by flip-chip bonding a hollowed out diamond box containing hermetically sealed platinum feedthroughs to the diamond array. The

subsequent device (Figure 4b), consists of a bottom diamond electrode array plate and top diamond box and houses the capacitors and ASIC devices. Following this step, the device is laser trimmed into the desired dimension ( $4 \times 4$  mm), and sealed with a laser weld as illustrated (Figure 4c). Flip-chip bonding the diamond box to the diamond array provides electrical pathways through the diamond encapsulation using the hermetically sealed platinum feedthroughs for interconnects to the outside world for power and data as depicted in Figure 4d. Here, a bundle of platinum wires are laser welded to the platinum feedthroughs exiting the back of the diamond box, to connect the encapsulated ASIC device to the external driving circuitry. Further information on the device performance is presented in the Supporting Information.

The planar hermetic diamond electrode array permits direct connection of the ASIC but, like all traditional integrated circuit components, the ASIC needs to be completely encapsulated to survive implantation. To best match material characteristics such as biocompatibility and thermal expansion between the array and the box, the remainder of the encapsulation was fabricated diamond in its polycrystalline structure (PCD). PCD is pinhole free and hermetic, but at the outset, no method existed to hermetically seal a diamond capsule while ensuring a long device lifetime (in excess of a decade) and at the same time not exceeding the temperature at which the ASIC would be damaged. A method was developed employing ABA.<sup>[35]</sup> ABAs are a family of alloys that contain a metal that can chemically react with the target substrate and form a strong bond. ABAs designed to bond diamond contain a carbide-forming metal such as titanium, chromium, or vanadium. Silver based ABAs are often used to secure diamond grit to metal shafts for cutting tool applications but silver has a poor biocompatibility and biostability profile. Therefore, a gold (96.4%) based ABA was selected to hermetically join the diamond array and box. The diamond box and array were fabricated with an annulus of Au-ABA around the closing edge of the parts. These parts were positioned together and the braze annuli were laser welded to each other to form a capsule with an internal volume of  $5.8 \times 10^{-9}$  m<sup>3</sup>. Figure 5 shows images of the diamond array and box with gold annuli on the closing edges before (Figure 5a) and during (Figure 5b) laser welding. Figure 5c is an SEM image of a laser welded braze seam. No leakage of helium through successful weld seams could be detected at detection limit of  $10^{-11}$  mbar L min<sup>-1</sup>.

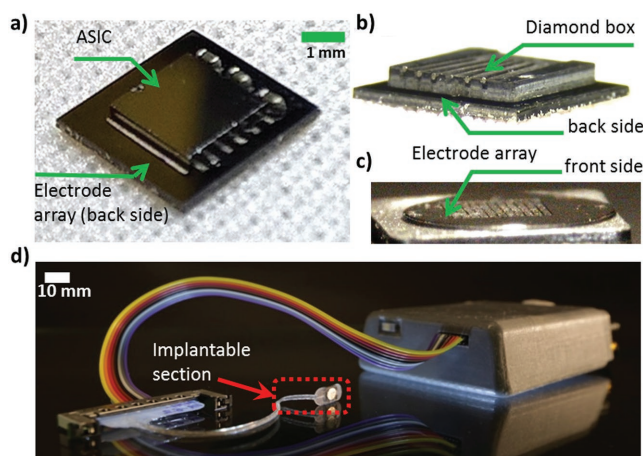


**Figure 4.** An overview of the diamond encapsulated implant integration and packing. a) Partially assembled device, consisting of diamond electrode array supporting a flip-chip bonded ASIC soldered on capacitors. Note: the reverse side of the electrode array is visible. b) The diamond box (top), see Figure 3a, is flip-chip bonded to the diamond electrode array (bottom) forming the full diamond capsule. Hermetically sealed platinum vertical vias embedded in the diamond box connect the encapsulated ASIC to the outside world via an external driver. c) Side view image of a diamond retinal prosthesis after the excess diamond shelf is trimmed. The front side of the electrode array is visible, which acts as the tissue–prosthesis interface. d) A bundle of platinum wires are used to connect the implant to the external driver circuitry.

## 5. The Diamond Stimulator is Able to Deliver Localized Charge

A key attribute of an epiretinal implant for high acuity is the ability to deliver localized charge stimuli to retinal ganglion cells. The degree of charge localization is influenced by the geometric form factors of the implant with respect to the retina, as well as the stimulation strategy. Parameters such as electrode size and pitch, electrode–target cell separation, and stimulating current pulse shape and stimulating/returning cell configuration influence the charge localization. The design strategy adopted in this work addresses some of these key challenges by facilitating the realization of a device with high density and

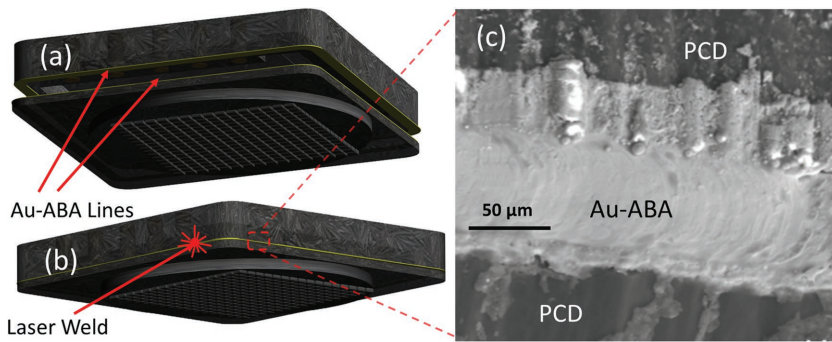


**Figure 5.** A hermetically sealed diamond box containing the stimulator chip is made possible by laser welding a gold ABA seam. a,b) Illustration of polished inlaid braze annuli indicating how the two parts fit together and are subsequently laser welded to form a hermetic seam. c) SEM image of a finished laser weld between two diamond components.

a high-count electrode array, in a hermetically sealed package that can take advantage of the full flexibility of the specially designed ASIC chip.

The efficacy of the diamond stimulator to deliver localized charge was assessed by measuring the spatial variation of voltage response in physiological saline solution. Here, one of the electrodes was driven using a biphasic pulse (100  $\mu$ A) in a bipolar configuration with a second diamond electrode acting as a return electrode. A third high

impedance voltage probe electrode with a tip diameter of  $\approx 10 \mu\text{m}$  was scanned along the surface in the lateral direction (in the saline solution at an approximate in-plane height of 100  $\mu\text{m}$ ) and above the electrode in the vertical (out-of-plane) direction. The measured voltage is relative to a large platinum reference electrode placed in the saline solution at a position  $\approx 1 \text{ cm}$  from the electrode. Assuming spatially homogenous saline conductance, the measured voltage at the probe electrode corresponds linearly to the current density at the given location. The lateral spatial variation of the measured voltage generated using 10  $\mu\text{m}$  step size is depicted in **Figure 6a**. The voltage magnitude is highest close to the active electrode

and drops as the distance increases in the lateral direction. This effect is best illustrated in **Figure 6b** (from the line-trace of **Figure 6a**), where a 50% drop in the voltage is recorded at  $\approx 100 \mu\text{m}$  from the electrode edge. A distance-dependent spread of current can also be observed in the vertical direction, relative to the plane of the electrode, as illustrated in the inset of **Figure 6b**, pointing to the importance of the implant placement.

The current localization illustrated in **Figure 6a,b** can be used to generate patterns using multiple stimulating

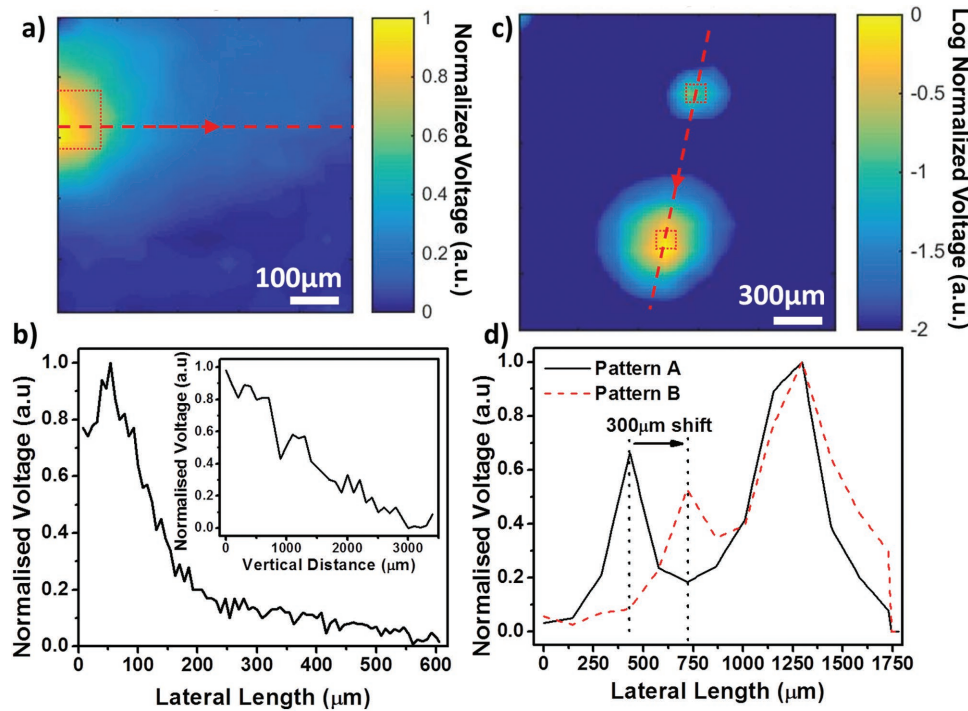


**Figure 6.** Voltage spread map at the vicinity of stimulating electrodes. a) Lateral (in-plane) voltage probe scan proximal to an active electrode. Red arrow represents the line-trace direction and location. The peak-to-peak voltage of the biphasic stimulus at each point in the saline normalized to the maximal response is presented. b) Line-trace of the normalized voltage as a function of the lateral distance (in-plane). Inset is the voltage dependence of the vertical (out-of-plane) distance above the electrode location. c) A pattern generated using two active electrodes (pattern A) with an 800  $\mu\text{m}$  interelectrode spacing between the active electrodes. Red box represents the position and size of the electrodes. Note: logarithmic scale bar is used here to represent voltage for better clarity. d) Line-trace of the generated pattern A, and comparison with a shifted pattern (pattern B), where the interelectrode spacing was reduced by 225  $\mu\text{m}$ .

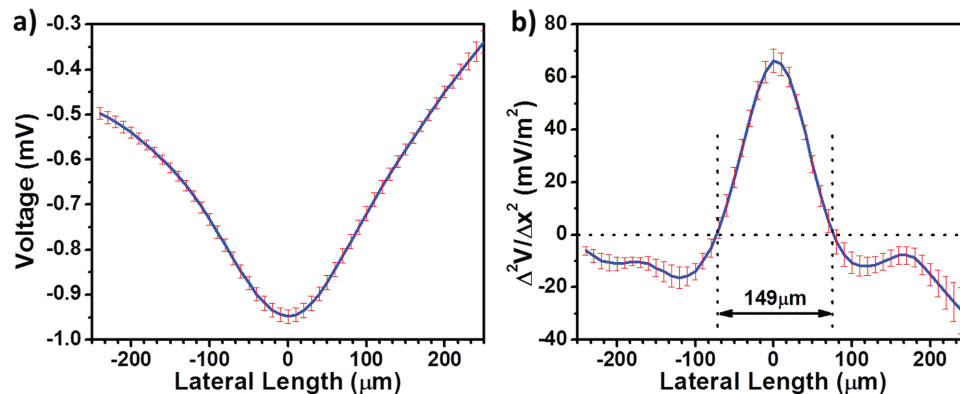


**Figure 7.** Spatial map of stimulation variability using N-UNCD electrodes. a) Average and standard deviation of the scanning voltage probe in the lateral plane at a nominal height of 50  $\mu\text{m}$  from the face of the electrode array for five different stimulating electrodes. b) The second-order spatial derivative of voltage-length shown in (a), which is proportional to the activating function and indicates the 149  $\mu\text{m}$  spatial extent of stimulation activity.

electrodes using a biphasic pulse train with pulse width of 1 ms and amplitude of 50  $\mu\text{A}$ . A simple pattern generated using two active electrodes with  $\approx 800$   $\mu\text{m}$  target spacing (pattern A) is shown in Figure 6c. The two active electrodes illustrated here can be clearly distinguished, and the  $\approx 800$   $\mu\text{m}$  spacing between the active electrodes can be reduced by using the ASIC to activate different electrodes. For instance, reducing the separation of the active electrode by 225  $\mu\text{m}$  (pattern B), resulted in a  $\approx 300$   $\mu\text{m}$  shift in the spacing of the two voltage peaks, as illustrated in the line-trace plot of voltage distance in Figure 6d.

The aforementioned scanning probe measurement was repeated at five different electrodes within the 256 electrode array using the same stimulation parameters and measurement setup described earlier. Figure 7a illustrates the average and standard error of the mean of the measured voltages for five different electrodes in the lateral plane at a nominal height of 50  $\mu\text{m}$  from the face of the electrode array. The second-order spatial derivative of the voltage-length plot shown (Figure 7a) can be used to assess the spatial localization of the stimulation in the 50  $\mu\text{m}$  plane. This second-order spatial derivative,  $\Delta^2 V/\Delta x^2$  shown in Figure 7b, is proportional to the activating function used to estimate the spatial extent of neuronal depolarization (or hyperpolarization) caused by electrical stimulation of the axons.<sup>[37–39]</sup> Axons rather than cell bodies are known to be the primary target of direct electrical stimulation in general and in retinal ganglion cells in particular.<sup>[40,41]</sup> The width of the positive peak of  $\Delta^2 V/\Delta x^2$  shown in Figure 7b during a cathodic stimulation pulse was 149  $\mu\text{m}$ . This is consistent with the 120  $\mu\text{m}$  square diamond electrodes, with a pitch of 150  $\mu\text{m}$  used in this work. The asymmetry in the shape of the curve can be attributed to the spatial configuration of return electrode in relation to the active electrode.

## 6. Biocompatibility of N-UNCD Adjacent to Retina

A requirement for high acuity prosthetic vision is that non-encapsulated materials, in particular the electrodes, must not cause any (or minimal) inflammatory response in the

surrounding tissues. Though we have previously assessed various forms of diamond for biocompatibility in vitro<sup>[42]</sup> and in muscle,<sup>[43]</sup> the unique immune-privileged environment of the eye requires a separate investigation. To assess the potential for N-UNCD to cause inflammation or cell death when placed adjacent to the retina, 1 mm diameter discs of 40  $\mu\text{m}$  thick N-UNCD were implanted in a subretinal location into ProHis23 rats. A subretinal, as opposed to an epiretinal location was chosen to hold the diamond disc in place. ProHis23 rats were chosen for this study, as they are an animal model for autosomal dominant retinitis pigmentosa.<sup>[44,45]</sup> The procedures for this study were approved by the Animal Research Ethics Committee of the University of Melbourne and complied with both the “Australian Code of Practice for the Care and Use of Animals for Scientific Purposes” and the “Principles of Laboratory Animal Care” for the use of animals in research. Like patients with autosomal dominant RP, ProHis23 rats carry a single amino acid substitution in the rod photoreceptor photopigment, rhodopsin, which causes gradual loss of rods followed by cones.<sup>[46]</sup> Further information on the experimental method is provided in the Supporting Information.

Figure 8a shows a typical fundus image of an N-UNCD implant under the rat retina. The subsequent panels in Figure 8 show vertical sections of the retina taken from a location away from the implant (control) and adjacent to the implant. Figure 8b,c shows vertical sections stained with the immunohistochemical markers calretinin (Calret, green), which labels ganglion and amacrine cells, and protein kinase C $\alpha$  (PKC, red), which labels rod bipolar cells. For all samples assessed using Calret and PKC, the inner retinal layers remained intact and there were no significant differences between the numbers of healthy cell phenotypes between controls and N-UNCD locations. Figure 8d,e shows vertical retinal sections stained for dying cells (TUNEL, green) and cell nuclei (ToPro, red). Dying cells were apparent in the remaining photoreceptor layer of the ProHis23 rats, consistent with the retinal degeneration phenotype, however there was no difference between control and N-UNCD locations. In addition, there was no cell death in the inner nuclear layer or ganglion cell layer in the N-UNCD areas. We conclude that N-UNCD

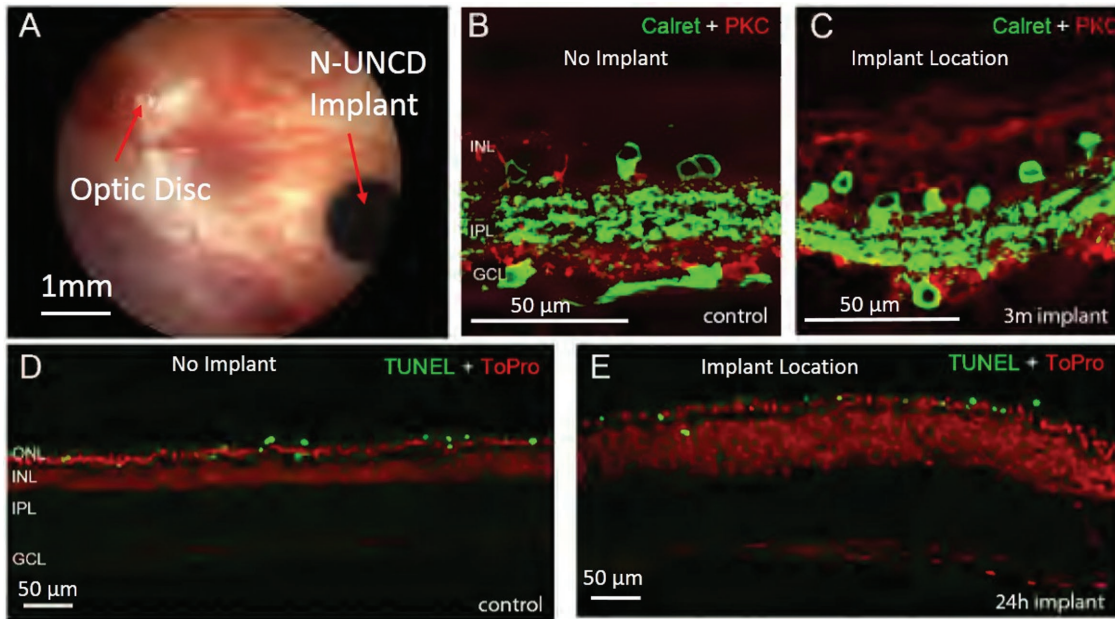


**Figure 8.** In vivo biocompatibility of the diamond implant. a) Fundus image of an adult ProHis23 rat showing a 1 mm diameter disc of N-UNCD after subretinal implantation for three months. b,c) Vertical sections of retina immunohistochemically stained with the neuronal markers, calretinin (Calret, green) and protein kinase C (PKC, red). d,e) Vertical sections of retina labeled for the cell death marker, TUNEL, and cell nuclei counterstained with ToPro.

is noncytotoxic and a biochemically safe material for use in a retinal implant.

## 7. Discussion

Earlier works have demonstrated that N-UNCD exhibits some of the key electrochemical<sup>[47]</sup> and biocompatibility<sup>[43]</sup> properties required for safe and long-term stimulation of retinal cells using electrodes with dimensions of  $\approx 100 \mu\text{m}$  or less. Indeed, retinal electrodes have been shown to excite retinal ganglion cells in rats<sup>[48]</sup> and to generate responses in vivo in the visual cortex of cats.<sup>[49]</sup> As well as validating noncytotoxicity and a biochemical safety of N-UNCD for use in a retinal implant, the present work demonstrates a diamond stimulator using an array of 256 N-UNCD microelectrodes.

Discounting inhomogeneous current spread within the retina, the potential acuity generated by a stimulator depends primarily on one factor – the ability of the electrode array to generate discrete electric fields above the stimulation thresholds of retinal ganglion cells in areas above the electrodes with minimal overlap. How the generated electric field interacts with the retina depends on a number of secondary factors including the distance from the retina, the amount of charge required, and the propensity of charge to dissipate or spread in the vitreous humor. In our preliminary work (as also noted by others<sup>[50]</sup>), there is a clear correlation between increased stimulation threshold and increased electrode distance from the retina.<sup>[49]</sup>

The voltage probe measurements depicted in Figures 6 and 7 indicate that the diamond stimulator demonstrated in this work is capable of generating  $\approx 150 \mu\text{m}$  regions of stimulation if the

device is positioned within  $50 \mu\text{m}$  of the retina. Though we have made significant steps toward a stable epiretinal attachment using magnets, ongoing work relating to the epiretinal device's shape relative to the retina (form factor) and other attachment techniques is required to ensure a long-term consistent and small separation between the array and the retina. As highlighted in Figure 7b, the confinement of current spread achieved here approaches that of the electrode dimensions, and can in principle be used to convey information to the retinal cells at acceptable acuities. In this first generation device, our results suggest that spatial resolution of  $\approx 150 \mu\text{m}$  is possible, which based on geometric approximation on human retina is equivalent to acuity of 20/660, and an  $8.8^\circ$  visual field for 256 electrodes.<sup>[17]</sup> In comparison, applying the same approximation to the Argus II epiretinal stimulator of Second Sight, consisting of 60 electrodes with diameters of  $200 \mu\text{m}$  and estimated pitch of  $542 \mu\text{m}$ ,<sup>[51]</sup> an acuity of 20/2420 is achievable. The best acuity observed during the Argus II patient trials was 20/1262.<sup>[52]</sup> Significantly, the technology used to demonstrate this generation of all-diamond stimulators is highly scalable in terms of electrode density and count, addressing the limitations posed by the conventional lateral fan-out interconnects used in many stimulators. The technology allows reduction in the electrode dimensions to 10–20  $\mu\text{m}$ , and increases the electrode numbers to  $10^6$  electrodes.<sup>[53,54]</sup> From a purely geometric approximation, this improvement equates to scaling of acuity to the 20/40–20/80 range and a visual field in excess of  $20^\circ$ .

The diamond stimulator is driven by a state-of-the-art ASIC device (Figure 2). The ASIC offers flexibility to deliver a wide variety of current pulse regimes including opposing or asynchronous phases during bipolar stimulation on adjacent or arbitrary combinations of electrodes. Although the measurements

in Figure 6 and 7 were conducted with the ASIC in its simplest stimulation mode, i.e., single or dual electrode matched pulses, there is enormous potential to shape the electric field above the array through current steering, using the cross-talk between electrodes to build complex stimulation patterns or to decrease the current spread from single electrodes. Furthermore, the integration of an N-UNCD electrode with the ASIC utilizes highly reliable and mature technologies that are readily scalable. Indeed, an electrode pitch size of 20  $\mu\text{m}$ <sup>[55]</sup> is commonly used at industrial scales, while electrode pitches of 8–10  $\mu\text{m}$ <sup>[53]</sup> have been demonstrated at small scales with a total electrode count in the order of 10<sup>6</sup>. This combination of flexible stimulation strategy combined with the demonstrated technology scalability in terms of electrode density and count paves the way for stimulation geometries comparable to that of a single cell. The reduction in per electrode footprint of the ASIC is expected to be accompanied with either a corresponding reduction in the area occupied by the electrode-driver circuitry or increased capability of time multiplexing channels. This is mainly due to the fact that the increase in electrode density, or in the other word, smaller electrode feature sizes, leads to a reduction in the maximum deliverable charge per electrode, while the safe charge injection capacity of the material is expected to remain constant (250  $\mu\text{C cm}^{-2}$  for N-UNCD). This scaling means that in future generation of the ASIC, the electrode-driver circuit is required to deliver lower currents, which require correspondingly smaller transistor dimensions.

Based on the international pool of successful results, artificial vision generated by electrical stimulation offers a significant potential to enhance the lives of people living with some forms of blindness. Only the future will tell how far the potential of prosthetic vision will reach and exactly how good prosthetic vision will become. Ultimately, reports from human users of such devices are the only way to truly assess the effectiveness of an implant. The small electrode spacing and the flexibility of stimulation regimes that the device under discussion here offers makes it an ideal system for measuring the potential acuity achievable using electrical stimulation. Compared to stimulator device architectures based on planar “fan-out” tracks for connecting stimulating chips and electrodes (e.g., Second Sight’s Argus II<sup>[51]</sup>), our device offers seamless scalability in electrode density and counts, while the dedicated ASIC technology offers highly adaptable and versatile stimulation capabilities, unmatched by features offered by light driven photodiodes that stimulate electrodes (e.g., Pixium Vision’s PRIMA subretinal implant).

## 8. Conclusion

The current generation of electrically driven retinal prostheses have demonstrated the possibility of using electrical stimulation to provide vision, albeit at very low acuities. If the acuity delivered by such devices is to improve, new fabrication strategies and technologies enabling many more electrodes and a high degree of stimulation flexibility must be developed. The device we present in this article is a diamond capsule and electrode array with integrated stimulation electronics featuring 256 N-UNCD electrodes with a pitch size of 150  $\mu\text{m}$ . Integrating the

implant’s electronic modules with a diamond electrode array has resulted in a highly flexible and reprogrammable all-in-one high-acuity implant with a high level of electrode density. The stimulator chip offers a wide variety of stimulation regimes including opposite phase or asynchronous current pulses. Significantly, the technology used to demonstrate this generation of all-diamond stimulators is highly scalable in terms of electrode density and count, addressing the limitations posed by the conventional lateral fan-out interconnects used in many stimulators. Beyond these possibilities, improvements in stimulation strategy in which the temporal and spatial excitation of adjacent electrodes are optimized will further contribute to visual experience of retinal prosthesis users.

## Supporting Information

Supporting Information is available from the Wiley Online Library or from the author.

## Acknowledgements

A.A. and H.M. contributed equally to this work. The authors wish to thank Tamara Brawn for her outstanding management of the BVA high acuity program, and Owen Burns for silicone mold and lead wire development. D.J.G. was supported by an Australian Research Council (ARC) DECRA grant DE130100922. N.V.A. was supported by an MMI-CSIRO materials science PhD scholarship. This research was supported by the National Health and Medical Research Council (NHMRC, Project Grant 585440) and the ARC through its Special Research Initiative (SRI) in Bionic Vision Science and Technology grant to the Bionic Vision Australia (BVA).

Received: September 23, 2016

Revised: October 27, 2016

Published online: December 5, 2016

- [1] E. Zrenner, *Science* **2002**, 295, 1022.
- [2] M. S. Humayun, J. D. Dorn, L. da Cruz, G. Dagnelie, J.-A. Sahel, P. E. Stanga, A. V. Cideciyan, J. L. Duncan, D. Elliott, E. Filley, A. C. Ho, A. Santos, A. B. Safran, A. Arditi, L. V. Del Priore, R. J. Greenberg, Argus II Study Group, *Ophthalmology* **2012**, 119, 779.
- [3] K. Stingl, K. U. Bartz-Schmidt, D. Besch, C. K. Chee, C. L. Cottrill, F. Gekeler, M. Groppe, T. L. Jackson, R. E. MacLaren, A. Koitschev, A. Kusnyerik, J. Neffendorf, J. Nemeth, M. A. N. Naeem, T. Peters, J. D. Ramsden, H. Sachs, A. Simpson, M. S. Singh, B. Wilhelm, D. Wong, E. Zrenner, *Vision Res.* **2015**, 111, 149.
- [4] L. N. Ayton, P. J. Blamey, R. H. Guymer, C. D. Luu, D. A. X. Nayagam, N. C. Sinclair, M. N. Shivdasani, J. Yeoh, M. F. McCombe, R. J. Briggs, N. L. Opie, J. Villalobos, P. N. Dimitrov, M. Varsamidis, M. A. Petoe, C. D. McCarthy, J. G. Walker, N. Barnes, A. N. Burkitt, C. E. Williams, R. K. Shepherd, P. J. Allen, for the Bionic Vision Australia Research Consortium, *PLoS One* **2014**, 9, e115239.
- [5] R. Guymer, A. Brandli, C. Luu, L. Ayton, *Eye Brain* **2016**, 8, 15.
- [6] G. J. Chader, J. Weiland, M. S. Humayun, *Prog. Brain Res.* **2009**, 175, 317.
- [7] M. N. Shivdasani, C. D. Luu, R. Cicione, J. B. Fallon, P. J. Allen, J. Leuenberger, G. J. Suaning, N. H. Lovell, R. K. Shepherd, C. E. Williams, *J. Neural Eng.* **2010**, 7, 36008.

- [8] J. Villalobos, P. J. Allen, M. F. McCombe, M. Ulaganathan, E. Zamir, D. C. Ng, R. K. Shepherd, C. E. Williams, *Albrecht Von Graefes Arch. Klin. Exp. Ophthalmol.* **2012**, *250*, 399.
- [9] J. Villalobos, D. A. X. Nayagam, P. J. Allen, P. McKelvie, C. D. Luu, L. N. Ayton, A. L. Freemantle, M. McPhedran, M. Basa, C. C. McGowan, R. K. Shepherd, C. E. Williams, *Invest. Ophthalmol. Vis. Sci.* **2013**, *54*, 3751.
- [10] K. Stingl, K. U. Bartz-Schmidt, D. Besch, A. Braun, A. Bruckmann, F. Gekeler, U. Greppmaier, S. Hipp, G. Hörtdörfer, C. Kernstock, A. Koitschev, A. Kusnyerik, H. Sachs, A. Schatz, K. T. Stingl, T. Peters, B. Wilhelm, E. Zrenner, *Proc. R. Soc. B* **2013**, *280*, 20130077.
- [11] I. Reutsky-Gefen, L. Golan, N. Farah, A. Schejter, L. Tsur, I. Brosh, S. Shoham, *Nat. Commun.* **2013**, *4*, 1509.
- [12] S. Nirenberg, C. Pandarinath, *Proc. Natl. Acad. Sci. USA* **2012**, *109*, 15012.
- [13] I. Tochitsky, A. Polosukhina, V. E. Degtyar, N. Gallerani, C. M. Smith, A. Friedman, R. N. Van Gelder, D. Trauner, D. Kaufer, R. H. Kramer, *Neuron* **2014**, *81*, 800.
- [14] A. Polosukhina, J. Litt, I. Tochitsky, J. Nemargut, Y. Sychev, I. De Kouchkovsky, T. Huang, K. Borges, D. Trauner, R. N. Van Gelder, R. H. Kramer, *Neuron* **2012**, *75*, 271.
- [15] B. K. Andrasfalvy, B. V. Zemelman, J. Tang, A. Vaziri, *Proc. Natl. Acad. Sci. USA* **2010**, *107*, 11981.
- [16] Z.-H. Pan, Q. Lu, A. Bi, A. M. Dizhoor, G. W. Abrams, *Annu. Rev. Vis. Sci.* **2015**, *1*, 185.
- [17] D. Palanker, A. Vankov, P. Huie, S. Baccus, *J. Neural Eng.* **2005**, *2*, S105.
- [18] P. Hess, *J. Appl. Phys.* **2012**, *111*, 51101.
- [19] R. K. Roy, K.-R. Lee, *J. Biomed. Mater. Res., Part B: Appl. Biomater.* **2007**, *83*, 72.
- [20] L. Yang, B. W. Sheldon, T. J. Webster, *Biomaterials* **2009**, *30*, 3458.
- [21] C. Popov, W. Kulisch, J. P. Reithmaier, T. Dostalova, M. Jelinek, N. Anspach, C. Hammann, *Diamond Relat. Mater.* **2007**, *16*, 735.
- [22] *Implantable Neural Prostheses 2* (Eds: D. Zhou, E. Greenbaum), Springer, New York **2010**.
- [23] X. Xiao, J. Wang, C. Liu, J. A. Carlisle, B. Mech, R. Greenberg, D. Guven, R. Freda, M. S. Humayun, J. Weiland, O. Auciello, *J. Biomed. Mater. Res., Part B: Appl. Biomater.* **2006**, *77*, 273.
- [24] D. J. Garrett, W. Tong, D. A. Simpson, H. Meffin, *Carbon* **2016**, *102*, 437.
- [25] K. Ganesan, D. J. Garrett, A. Ahnood, M. N. Shivdasani, W. Tong, A. M. Turnley, K. Fox, H. Meffin, S. Prawer, *Biomaterials* **2014**, *35*, 908.
- [26] H. Lorach, G. Goetz, R. Smith, X. Lei, Y. Mandel, T. Kamins, K. Mathieson, P. Huie, J. Harris, A. Sher, D. Palanker, *Nat. Med.* **2015**, *21*, 476.
- [27] K. Mathieson, J. Loudin, G. Goetz, P. Huie, L. Wang, T. I. Kamins, L. Galambos, R. Smith, J. S. Harris, A. Sher, D. Palanker, *Nat. Photonics* **2012**, *6*, 391.
- [28] S. F. Cogan, *Annu. Rev. Biomed. Eng.* **2008**, *10*, 275.
- [29] D. Boinagrov, X. Lei, G. Goetz, T. I. Kamins, K. Mathieson, L. Galambos, J. S. Harris, D. Palanker, *IEEE Trans. Biomed. Circuits Syst.* **2016**, *10*, 85.
- [30] A. C. Weitz, M. R. Behrend, M. S. Humayun, R. H. Chow, J. D. Weiland, in *IEEE Engineering Medicine Biology Society*, IEEE, Piscataway, NJ, USA **2011**, pp. 6725–6728.
- [31] M. K. Cosetti, S. B. Waltzman, *Expert Rev. Med. Devices* **2011**, *8*, 389.
- [32] A. E. Krieger, *Trans. Am. Ophthalmol. Soc.* **1991**, *89*, 549.
- [33] N. Tran, S. Bai, J. Yang, H. Chun, O. Kavehei, Y. Yang, V. Muktamath, D. Ng, H. Meffin, M. Halpern, E. Skafidas, *IEEE J. Solid-State Circuits* **2014**, *49*, 751.
- [34] N. V. Apollo, D. Lau, A. Ahnood, A. Stacey, K. Ganesan, S. G. Lichter, K. Fox, J. Foroughi, H. Meffin, G. G. Wallace, R. Baughman, S. Prawer, D. J. Garrett, *Carbon* **2006**, *104*, 180.
- [35] S. G. Lichter, M. C. Escudie, A. D. Stacey, K. Ganesan, K. Fox, A. Ahnood, N. V. Apollo, D. C. Kua, A. Z. Lee, C. McGowan, A. L. Saunders, O. Burns, D. A. X. Nayagam, R. A. Williams, D. J. Garrett, H. Meffin, S. Prawer, *Biomaterials* **2015**, *53*, 464.
- [36] A. Ahnood, M. C. Escudie, R. Cicione, C. D. Abeyrathne, K. Ganesan, K. E. Fox, D. J. Garrett, A. Stacey, N. V. Apollo, S. G. Lichter, C. D. L. Thomas, N. Tran, H. Meffin, S. Prawer, *Biomed. Microdevices* **2015**, *17*, 1.
- [37] H. Meffin, B. Tahayori, E. N. Sergeev, I. M. Y. Mareels, D. B. Grayden, A. N. Burkitt, *J. Neural Eng.* **2014**, *11*, 65004.
- [38] H. Meffin, B. Tahayori, D. B. Grayden, A. N. Burkitt, *J. Neural Eng.* **2012**, *9*, 65005.
- [39] F. Rattay, *Neuroscience* **1999**, *89*, 335.
- [40] S. I. Fried, A. C. W. Lasker, N. J. Desai, D. K. Eddington, J. F. Rizzo, *J. Neurophysiol.* **2009**, *101*, 1972.
- [41] L. G. Nowak, J. Bullier, *Exp. Brain Res.* **1998**, *118*, 489.
- [42] W. Tong, K. Fox, K. Ganesan, A. M. Turnley, O. Shimoni, P. A. Tran, A. Lohrmann, T. McFarlane, A. Ahnood, D. J. Garrett, H. Meffin, N. M. O'Brien-Simpson, E. C. Reynolds, S. Prawer, *Mater. Sci. Eng., C* **2014**, *43*, 135.
- [43] D. J. Garrett, A. L. Saunders, C. McGowan, J. Specks, K. Ganesan, H. Meffin, R. A. Williams, D. A. X. Nayagam, *J. Biomed. Mater. Res., Part B: Appl. Biomater.* **2016**, *104*, 19.
- [44] M. L. Acosta, Y.-S. Shin, S. Ready, E. L. Fletcher, D. L. Christie, M. Kalloniatis, *Am. J. Physiol.: Cell Physiol.* **2010**, *298*, C764.
- [45] E. L. Fletcher, A. I. Jobling, K. A. Vessey, C. Luu, R. H. Guymer, P. N. Baird, *Prog. Mol. Biol. Transl. Sci.* **2011**, *100*, 211.
- [46] E. L. Berson, B. Rosner, M. A. Sandberg, T. P. Dryja, *Arch. Ophthalmol. (Chicago, IL, USA)* **1991**, *109*, 92.
- [47] D. J. Garrett, K. Ganesan, A. Stacey, K. Fox, H. Meffin, S. Prawer, *J. Neural Eng.* **2012**, *9*, 16002.
- [48] A. E. Hadjinicolaou, R. T. Leung, D. J. Garrett, K. Ganesan, K. Fox, D. A. X. Nayagam, M. N. Shivdasani, H. Meffin, M. R. Ibbotson, S. Prawer, B. J. O'Brien, *Biomaterials* **2012**, *33*, 5812.
- [49] M. Shivdasani, D. Garrett, D. Nayagam, J. Villalobos, P. Allen, A. Saunders, M. McPhedran, C. McGowan, H. Meffin, R. Shepherd, *Invest. Ophthalmol. Vis. Sci.* **2013**, *54*, 1029.
- [50] C. de Balthasar, S. Patel, A. Roy, R. Freda, S. Greenwald, A. Horsager, M. Mahadevappa, D. Yanai, M. J. McMahon, M. S. Humayun, R. J. Greenberg, J. D. Weiland, I. Fine, *Invest. Ophthalmol. Vis. Sci.* **2008**, *49*, 2303.
- [51] J. D. Dorn, A. K. Ahuja, A. Caspi, L. Da Cruz, G. Dagnelie, J. A. Sahel, R. J. Greenberg, M. J. McMahon, *JAMA Ophthalmol.* **2013**, *131*, 183.
- [52] Interim Results from the International Trial of Second Sight's Visual Prosthesis - ClinicalKey, <https://www.clinicalkey.com-au.ezp.lib.unimelb.edu.au/#!/content/playContent/1-s2.0-S0161642011008840?returnurl=null&referrer=null> (accessed: October 2016).
- [53] J. John, L. Zimmermann, P. D. Moor, C. V. Hoof, *Nucl. Instrum. Methods Phys. Res., Sect. A* **2004**, *531*, 202.
- [54] A. W. Hoffman, P. J. Love, J. P. Rosbeck, *Proc. SPIE* **2003**, *5167*, 194.
- [55] P. J. Love, A. W. Hoffman, D. J. Gulbransen, M. P. Murray, K. J. Ando, N. J. Therrien, J. P. Rosbeck, R. S. Holcombe, *Proc. SPIE* **2003**, *5167*, 134.